JOURNAL OF ELECTROMAGNETIC ENGINEERING AND SCIENCE, VOL. 25, NO. 3, 279~290, MAY. 2025

https://doi.org/10.26866/jees.2025.3.r.298
ISSN 2671-7263 (Online) · ISSN 2671-7255 (Print)

Multi-Functional Filtering Power Divider with a Reconfigurable Frequency and Ultrawide Isolator Functionality

Girdhari Chaudhary[1] · Daewoo Choi[2,*] · Yongchae Jeong[1,3,*]

Abstract

In this paper, we describe the co-design of a multi-functional non-reciprocal filtering power divider (NR-FPD) with ultrawide reverse isolation and frequency reconfigurable functionality. The proposed NR-FPD offers an arbitrary power division ratio (PDR) with low transmission loss in the forward direction and non-reciprocal behavior along with an ultrawide high reverse isolation bandwidth in the backward direction. For a better understanding of the behavior of the proposed NR-FPD, analytical equations of spectral S-parameters were derived. These equations allowed for the selection of optimum circuit and modulation parameters without the need for harmonic balance simulation. The ultrawide high reverse isolation bandwidth was achieved through the proper selection of optimum modulation parameters. For the proof of concept, the NR-FPD with an equal PDR was fabricated and characterized. Measurement results showed that the frequency was continuously tuned between 1.62 GHz to 1.95 GHz, and there was insertion loss of 5.70 dB in the forward direction of transmission and an ultrawide 20 dB isolation bandwidth in the backward direction of transmission.

Key Words: Frequency Reconfigurable, Non-Reciprocal Circuits, Non-reciprocal Power Divider, Spatio-temporal Modulation, Time-Modulated Resonators, Varactor Diode.

I. INTRODUCTION

Multi-functional microwave and millimeter wave circuits are essential components of next generation communication systems. Since emerging applications require multi-functional RF front ends, there is a pressing need for power dividers/combiners capable of accommodating these advancements [1, 2]. One promising approach for miniaturizing the RF front-end and enhancing functionality involves combining the power divider, tunable filter, and isolator functions into a single circuit. Circulators and isolators are widely used in measurement, communication, and radar systems [3]. However, conventional circulators and isolators are mainly designed using a ferrite magnetic material [4], which is expensive, bulky, and incompatible with integrated circuit (IC) design.

In recent years, the spatio-temporal modulation (STM) technique has been widely used to design non-reciprocal circuits without the use of magnetic materials. Non-reciprocal bandpass filters (NR-BPFs) that integrate functionalities of isolators and filters using time-modulated resonators have been explored [5–13]. The STM concept has also been utilized to design non-

---

Manuscript received June 21, 2024 ; Revised October 02, 2024 ; Accepted October 15, 2024. (ID No. 20240621-132J)

[1] Jeonbuk RICE Intelligence Innovation Research Center, Jeonbuk National University, Jeonju, Korea.
[2] The Graduate School of Convergence Technology Management, Jeonbuk National University, Jeonju, Korea.
[3] Division of Electronic Engineering and IT Convergence Research Center, Jeonbuk National University, Jeonju, Korea.
[*] Corresponding Author: Daewoo Choi (qorwkr@jbnu.ac.kr) and Yongchae Jeong (ycjeong@jbnu.ac.kr)

reciprocal power dividers (i.e., $|S_{21}| \neq |S_{12}|$ and $|S_{31}| \neq |S_{13}|$) by employing a combination of static and time-modulated resonators [14, 15]. In [16, 17], non-reciprocal filtering power dividers (NR-FPDs) with tunable frequencies were presented.

However, these designs require at least six time-modulated resonators. The aforementioned NR-BPFs and power dividers have achieved excellent reverse isolation only at the center frequency (f_0). In [6, 10–12], an NR-BPFs yielded reverse isolation values of up to 40 dB at f_0, however, the 20 dB reverse isolation bandwidth was very narrow. Similarly, NR-FPDs with improved isolation bandwidth have been presented in [16, 17]. However, the 20 dB isolation bandwidth of these NR-FPDs was in the range of 23–50 MHz.

This paper presents the design of a microstrip line NR-FPD that offers frequency tunable characteristics with ultrawide bandwidth isolator functionality. The proposed design features an equal and unequal power division ratio (PDR) with low transmission insertion loss (IL) and ultrawide high isolation in the backward direction. To achieve deep understanding of the proposed multi-functional NR-FPD's non-reciprocity behavior, the analytical spectral scattering parameters (*S*-parameters) of the microstrip line NR-FPD were derived. As a proof of concept, an equal PDR NR-FPD with ultrawide reverse isolation bandwidth and tunable frequency functionality was designed, fabricated, and measured.

II. DESIGN THEORY

1. Proposed Transmission Line Time-Modulated Resonator

Fig. 1(a) depicts a schematic of time-modulated resonator. The proposed time-modulated resonators consisted of a transmission with characteristic admittances of Y_2, Y_1, and Y_b, and electrical lengths of θ_c, θ_1, θ_0, and θ_b. The capacitor $C_v(t)$ was modulated with a sinusoidal modulation signal as follows:

$$C_v(t) = C_{v0}[1 + \mathrm{m}\cos\{2\pi f_m t + (i-1)\Delta\varphi\}], \tag{1}$$

where f_m, $\Delta\varphi$, and m represent the modulation frequency, phase shift, and modulation index of the modulation signal [6], and C_{v0} denotes nominal capacitance. The modulation of the resonator with the sinusoidal signal resulted in intermodulation (IM) products at harmonic frequencies (i.e., $\omega + k\omega_m$ where k_i = ⋯, −2, -1, 0, +1, +2, ⋯). If the number of harmonics was N_{har}, then the input spectral admittance matrix of an i^{th} transmission time-modulated resonator was written as (2),

$$Y_{in,i}^{(p_1,p_2)} = j\begin{bmatrix} \cdots & \cdots & \cdots & \cdots & \cdots & \cdots \\ B^{-2} & x^{-2}\frac{m}{2}C_{v0}e^{-j(i-1)\Delta\varphi} & 0 & 0 & 0 & \cdots \\ \cdots x^{-1}\frac{m}{2}C_{v0}e^{j(i-1)\Delta\varphi} & B^{-1} & x^{-1}\frac{m}{2}C_{v0}e^{-j(i-1)\Delta\varphi} & 0 & & \cdots \\ 0 & x^{0}\frac{m}{2}C_{v0}e^{j(i-1)\Delta\varphi} & B^{0} & x^{0}\frac{m}{2}C_{v0}e^{-j(i-1)\Delta\varphi} & 0 & \cdots \\ 0 & 0 & x^{+1}\frac{m}{2}C_{v0}e^{j(i-1)\Delta\varphi} & B^{+1} & x^{+1}\frac{m}{2}C_{v0}e^{-j(i-1)\Delta\varphi} & \cdots \\ 0 & 0 & 0 & x^{+2}\frac{m}{2}C_{v0}e^{j(i-1)\Delta\varphi} & B^{+2} & \cdots \\ \cdots & \cdots & \cdots & \cdots & \cdots & \cdots \end{bmatrix} \tag{2}$$

where $Y_{in,i}^{k_1,k_2}$ symbolizes the spectral admittance matrix at frequency components $\omega + k\omega_m$. The values of B^k, D_1, D_2, and x^k were expressed as follows:

$$B^n = Y_2\frac{D_1 + Y_2\tan\left(x^n\theta_c/\omega_{ref}\right)}{Y_2 - D_1\tan\left(x^n\theta_c/\omega_{ref}\right)}, \tag{3a}$$

$$D_1 = Y_1\frac{D_2 + Y_1\tan\left(x^n\theta_1/\omega_{ref}\right)}{Y_1 - D_2\tan\left(x^n\theta_1/\omega_{ref}\right)}, \tag{3b}$$

$$D_2 = \frac{x^n C_{v0} Y_1 \cot\left(x^n\theta_0/\omega_{ref}\right)}{Y_1\cot\left(x^n\theta_0/\omega_{ref}\right) - x^n C_{v0}} - Y_b\cot\left(\frac{x^n\theta_b}{\omega_{ref}}\right), \tag{3c}$$

$$x^n = \omega + n\omega_m, \qquad n = \cdots, -2, -1, 0, +1, +2, \cdots \tag{3d}$$

where ω_{ref} is an angular frequency at which the electrical length of transmission is chosen. As depicted in Eq. (2), it is important to emphasize that the spectral admittance matrix no longer held a singular value. The resonant frequency at the fundamental frequency (i.e., n = 0) was obtained by equating $im\left(Y_{in,i}^{0,0}\right)$ to zero.

2. Spectral S-Parameters

Fig. 1(b) shows a schematic of the NR-FPD with an arbitrary PDR, comprised of admittance inverters and time-modulated resonators. The RF ports of the NR-FPD were terminated with the admittance of $Y_0 = 1/Z_0 = 0.02\ \Omega$. To determine the spectral *S*-parameters of the proposed NR-FPD, modified even- and odd-mode analysis methods were adapted. Assuming that the input signal was divided between the output ports in a ratio of $1{:}\,k^2$, the spectral *S*-parameters of the entire circuit were expressed in terms of the even- and odd-mode *S*-parameters, as follows:

$$[\mathbf{S}] = \begin{bmatrix} \mathbf{S}_{11e}^{(p_1,p_2)} & \frac{k\mathbf{S}_{12e}^{(p_1,p_2)}}{\sqrt{1+k^2}} & \frac{\mathbf{S}_{13e}^{(p_1,p_2)}}{\sqrt{1+k^2}} \\ \frac{k\mathbf{S}_{21e}^{(p_1,p_2)}}{\sqrt{1+k^2}} & \frac{k^2\left(\mathbf{S}_{22e}^{(p_1,p_2)} + \mathbf{S}_{22o}^{(p_1,p_2)}\right)}{1+k^2} & \frac{\mathbf{S}_{22e}^{(p_1,p_2)} - \mathbf{S}_{22o}^{(p_1,p_2)}}{2} \\ \frac{\mathbf{S}_{31e}^{(p_1,p_2)}}{\sqrt{1+k^2}} & \frac{\mathbf{S}_{33e}^{(p_1,p_2)} - \mathbf{S}_{33o}^{(p_1,p_2)}}{2} & \frac{\mathbf{S}_{11e}^{(p_1,p_2)} + \mathbf{S}_{33o}^{(p_1,p_2)}}{1+k^2} \end{bmatrix} \tag{4}$$

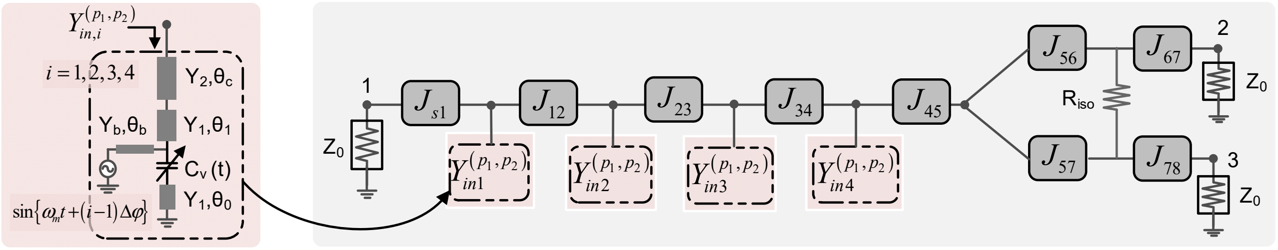

(a) (b)

Fig. 1. Proposed structure: (a) a time-modulated resonator and (b) an NR-FPD with microstrip line time-modulated resonators and admittance inverters.

As seen in Eq. (4), the S-parameter $\boldsymbol{S}_{i,j}^{(p_1,p_2)}$ did not possess a single value. Instead, it represented a spectral harmonic scattering matrix at the frequency of interest. For example, $\boldsymbol{S}_{21}^{(0,0)}=S_{21}$ presented a transmission scattering parameter at port 2 at a fundamental frequency.

Figs. 2 and 3 show equivalent schematics for ports 2 and 1, and ports 3 and 1, respectively, under even- and odd-mode excitations. Under the even-excitations, the port 1 impedance was divided into $\left(\frac{1+k^2}{k^2}\right)Z_0$ and $(1+k^2)Z_0$. However, this impedance was short-circuited under the odd-mode excitation. Similarly, the input admittance of time-modulated resonators was divided into $\left(\frac{k^2}{1+k^2}\right)Y_{in,i}^{(p_1,p_2)}$ and $\left(\frac{1}{1+k^2}\right)Y_{in,i}^{(p_1,p_2)}$. Using equivalent circuits, as depicted in Fig. 2, the even- and odd-mode spectral S-parameters between ports 2 and 1 were expressed in the following equations, where U is unitary matrix.

$$\mathbf{S}_{11e}^{(p_1,p_2)}=\mathbf{S}_{22e}^{(p_1,p_2)}=\\ U-\frac{2Z_0\mathbf{J}_{\mathbf{sl}}^2\begin{Bmatrix}k^2Z_0\mathbf{J}_{\mathbf{45}}^2\mathbf{J}_{\mathbf{67}}^2A_3\\+(1+k^2)\mathbf{J}_{\mathbf{56}}^2A_4\end{Bmatrix}}{\begin{Bmatrix}k^2Z_0\mathbf{J}_{\mathbf{45}}^2\mathbf{J}_{\mathbf{67}}^2A_1+(1+k^2)\mathbf{J}_{\mathbf{56}}^2A_2\\+k^2Z_0^2\mathbf{J}_{\mathbf{sl}}^2\mathbf{J}_{\mathbf{45}}^2\mathbf{J}_{\mathbf{67}}^2A_3\\+(1+k^2)Z_0\mathbf{J}_{\mathbf{s1}}^2\mathbf{J}_{\mathbf{56}}^2A_4\end{Bmatrix}}, \tag{5a}$$

$$\mathbf{S}_{22o}^{(p_1,p_2)}=\frac{U-R_{iso}^{21}Z_0\mathbf{J}_{\mathbf{67}}^{\mathbf{2}}}{U+R_{iso}^{21}\mathbf{J}_{\mathbf{67}}^{\mathbf{2}}}, \tag{5b}$$

$$\mathbf{S}_{21e}^{(p_1,p_2)}=\\ \frac{\sqrt{1+k^2}}{k}\frac{2k^2Z_0\mathbf{J}_{\mathrm{sl}}\mathbf{J}_{12}\mathbf{J}_{23}\mathbf{J}_{34}\mathbf{J}_{45}\mathbf{J}_{56}\mathbf{J}_{67}}{\begin{Bmatrix}k^2\mathbf{J}_{45}^2\mathbf{J}_{67}^2A_1Z_0+(1+k^2)\mathbf{J}_{56}^2A_2\\+k^2Z_0^2\mathbf{J}_{\mathrm{sl}}^2\mathbf{J}_{56}^2\mathbf{J}_{67}^2A_3+(1+k^2)Z_0\mathbf{J}_{\mathrm{sl}}^2\mathbf{J}_{56}^2A_4\end{Bmatrix}}, \tag{5c}$$

$$\mathbf{S}_{12e}^{(p_1,p_2)}=\\ \frac{\sqrt{1+k^2}}{k}\frac{2k^2Z_0\mathbf{J}_{\mathrm{sl}}\mathbf{J}_{12}\mathbf{J}_{23}\mathbf{J}_{34}\mathbf{J}_{45}\mathbf{J}_{56}\mathbf{J}_{67}}{\begin{Bmatrix}k^2\mathbf{J}_{45}^2\mathbf{J}_{67}^2B_1Z_0+(1+k^2)\mathbf{J}_{56}^2B_2\\+k^2Z_0^2\mathbf{J}_{51}^2\mathbf{J}_{45}^2\mathbf{J}_{67}^2B_3+(1+k^2)Z_0\mathbf{J}_{51}^2\mathbf{J}_{56}^2B_4\end{Bmatrix}} \tag{5d}$$

Similarly, Fig. 3 depicts equivalent circuits between ports 3 and 1 when even- and odd-mode excitations were applied. Using these equivalent circuits, even- and odd-mode spectral reflection and transmission coefficients were derived as follows:

$$\mathbf{S}_{33e}^{(p_1,p_2)}=\\ U-\frac{2Z_0\mathbf{J}_{\mathbf{sl}}^2\{Z_0\mathbf{J}_{\mathbf{45}}^2\mathbf{J}_{\mathbf{78}}^2A_3+(1+k^2)Z_0\mathbf{J}_{\mathbf{57}}^2A_4\}}{\begin{Bmatrix}Z_0\mathbf{J}_{\mathbf{45}}^2\mathbf{J}_{\mathbf{78}}^2A_1+(1+k^2)\mathbf{J}_{\mathbf{57}}^2A_2\\+Z_0^2\mathbf{J}_{\mathbf{sl}}^2\mathbf{J}_{\mathbf{45}}^2\mathbf{J}_{\mathbf{78}}^2A_3+(1+k^2)Z_0\mathbf{J}_{\mathbf{sl}}^2\mathbf{J}_{\mathbf{57}}^2A_4\end{Bmatrix}}, \tag{6a}$$

$$\mathbf{S}_{31e}^{(p_1,p_2)}=\frac{2Z_0\sqrt{1+k^2}\mathbf{J}_{\mathbf{s1}}\mathbf{J}_{\mathbf{12}}\mathbf{J}_{\mathbf{23}}\mathbf{J}_{\mathbf{34}}\mathbf{J}_{\mathbf{45}}\mathbf{J}_{\mathbf{57}}\mathbf{J}_{\mathbf{78}}}{\begin{Bmatrix}Z_0\mathbf{J}_{\mathbf{45}}^2\mathbf{J}_{\mathbf{78}}^2A_1+(1+k^2)\mathbf{J}_{\mathbf{57}}^2A_2\\+Z_0^2\mathbf{J}_{\mathbf{sl}}^2\mathbf{J}_{\mathbf{45}}^2\mathbf{J}_{\mathbf{78}}^2A_3+(1+k^2)Z_0\mathbf{J}_{\mathbf{sl}}^2\mathbf{J}_{\mathbf{57}}^2A_4\end{Bmatrix}}, \tag{6b}$$

$$\mathbf{S}_{13e}^{(p_1,p_2)}=\\ \frac{2Z_0\sqrt{1+k^2}\mathbf{J}_{\mathbf{s1}}\mathbf{J}_{\mathbf{12}}\mathbf{J}_{\mathbf{23}}\mathbf{J}_{\mathbf{34}}\mathbf{J}_{\mathbf{45}}\mathbf{J}_{\mathbf{57}}\mathbf{J}_{\mathbf{78}}}{\begin{Bmatrix}k^2\mathbf{J}_{\mathbf{45}}^2\mathbf{J}_{\mathbf{78}}^2B_1Z_0+(1+k^2)\mathbf{J}_{\mathbf{57}}^2B_2\\+k^2Z_0^2\mathbf{J}_{\mathbf{s1}}^2\mathbf{J}_{\mathbf{45}}^2\mathbf{J}_{\mathbf{78}}^2B_3+(1+k^2)Z_0\mathbf{J}_{\mathbf{s1}}^2\mathbf{J}_{\mathbf{57}}^2B_4\end{Bmatrix}}, \tag{6c}$$

$$\mathbf{S}_{33o}^{(p_1,p_2)}=\frac{U-R_{iso}^{31}Z_0\mathbf{J}_{\mathbf{78}}^2}{U+R_{iso}^{31}Z_0\mathbf{J}_{\mathbf{78}}^2}. \tag{6d}$$

The values of A_i and B_i were expressed as follows:

$$A_1=\\ \mathbf{J}_{12}^2Y_{in3}^{(p_1,p_2)}+\mathbf{J}_{23}^2Y_{in1}^{(p_1,p_2)}+Y_{in1}^{(p_1,p_2)}Y_{in2}^{(p_1,p_2)}Y_{in3}^{(p_1,p_2)}, \tag{7a}$$

$$A_2=\\ \begin{Bmatrix}\mathbf{J}_{12}^2\mathbf{J}_{34}^2+\mathbf{J}_{12}^2Y_{in3}^{(p_1,p_2)}Y_{in4}^{(p_1,p_2)}+\mathbf{J}_{23}^2Y_{in1}^{(p_1,p_2)}Y_{in4}^{(p_1,p_2)}\\+\mathbf{J}_{34}^2Y_{in1}^{(p_1,p_2)}Y_{in2}^{(p_1,p_2)}+Y_{in1}^{(p_1,p_2)}Y_{in2}^{(p_1,p_2)}Y_{in3}^{(p_1,p_2)}Y_{in4}^{(p_1,p_2)}\end{Bmatrix} \tag{7b}$$

$$A_3=\mathbf{J}_{23}^2+Y_{in2}^{(p_1,p_2)}Y_{in3}^{(p_1,p_2)}, \tag{7c}$$

$$A_4=\\ \mathbf{J}_{23}^2Y_{in4}^{(p_1,p_2)}+\mathbf{J}_{34}^2Y_{in2}^{(p_1,p_2)}+Y_{in2}^{(p_1,p_2)}Y_{in3}^{(p_1,p_2)}Y_{in4}^{(p_1,p_2)}, \tag{7d}$$

$$B_1=\\ \mathbf{J}_{12}^2Y_{in3}^{(p_1,p_2)}+\mathbf{J}_{23}^2Y_{in1}^{(p_1,p_2)}+Y_{in3}^{(p_1,p_2)}Y_{in2}^{(p_1,p_2)}Y_{in1}^{(p_1,p_2)}, \tag{7e}$$

$$B_2=\\ \begin{Bmatrix}\mathbf{J}_{12}^2\mathbf{J}_{34}^2+\mathbf{J}_{12}^2Y_{in4}^{(p_1,p_2)}Y_{in3}^{(p_1,p_2)}+\mathbf{J}_{23}^2Y_{in4}^{(p_1,p_2)}Y_{in1}^{(p_1,p_2)}\\+\mathbf{J}_{34}^2Y_{in2}^{(p_1,p_2)}Y_{in1}^{(p_1,p_2)}+Y_{in4}^{(p_1,p_2)}Y_{in3}^{(p_1,p_2)}Y_{in2}^{(p_1,p_2)}Y_{in1}^{(p_1,p_2)}\end{Bmatrix} \tag{7f}$$

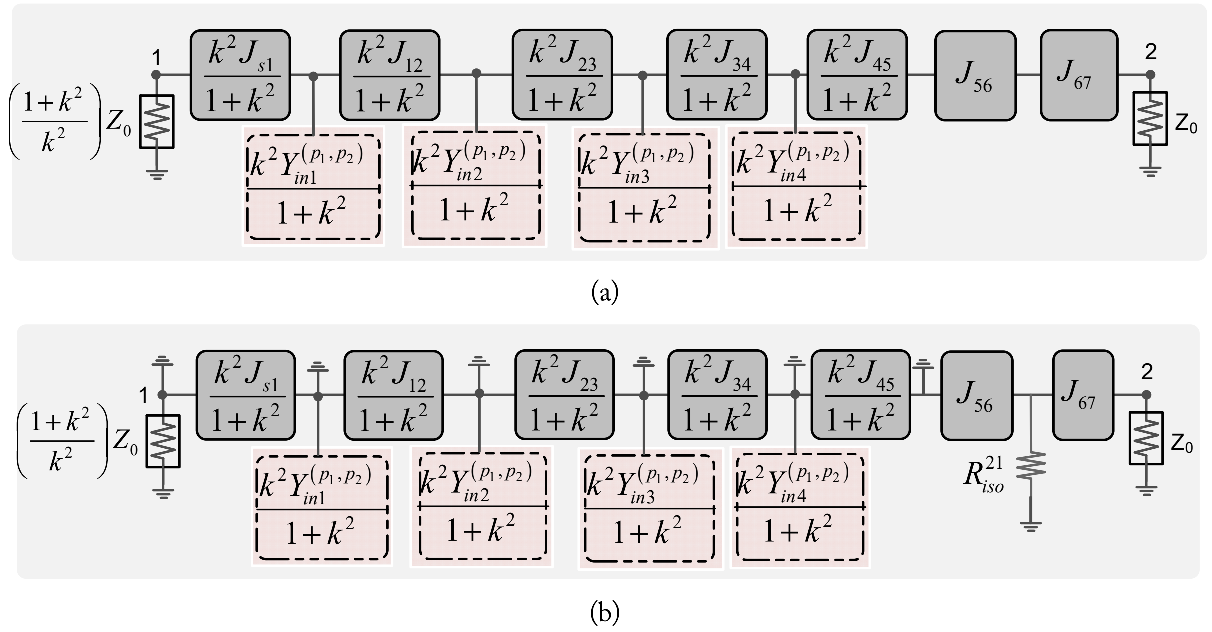

(a)

(b)

Fig. 2. Even- and odd-mode equivalent circuits between ports 2 and 1: (a) an even-mode equivalent circuit and (b) an odd-mode equivalent circuit.

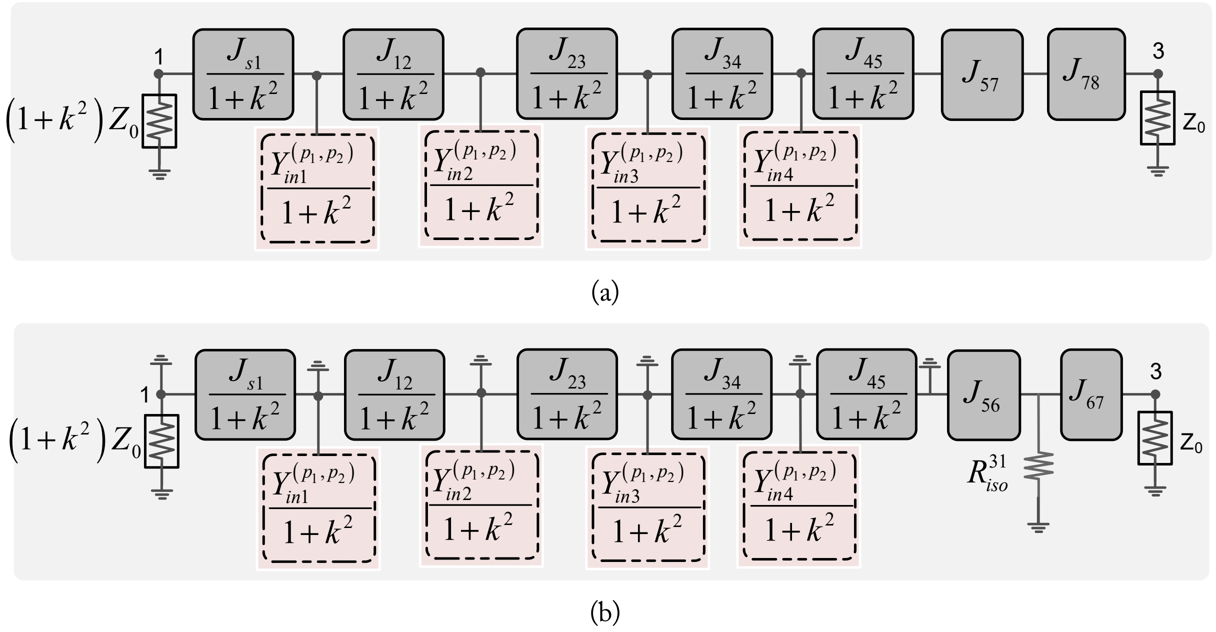

(a)

(b)

Fig. 3. Equivalent circuits under even- and odd-mode excitations between ports 3 and 1: (a) an even-mode equivalent circuit and (b) an odd-mode equivalent circuit.

$$B_3 = \mathbf{J}_{23}^2 + Y_{in3}^{(p_1,p_2)} Y_{in2}^{(p_1,p_2)}, \tag{7g}$$

$$B_4 = \mathbf{J}_{23}^2 Y_{in4}^{(p_1,p_2)} + \mathbf{J}_{34}^2 Y_{in2}^{(p_1,p_2)} + Y_{in4}^{(p_1,p_2)} Y_{in3}^{(p_1,p_2)} Y_{in2}^{(p_1,p_2)}. \tag{7h}$$

It should be noted that admittance inverters (J-inverters) value remained same as they were without modulation (i.e., in the static state) [6, 8]. The J-inverter values were expressed as follows:

$$\mathbf{J}_{s1} = \sqrt{\frac{\Delta b_1^{(0,0)} U}{Z_0 g_0 g_1}}, \quad \mathbf{J}_{45} = \sqrt{\frac{\Delta b_4^{(0,0)} U}{Z_0 g_4 g_5}}, \tag{8a}$$

$$\mathbf{J}_{i,i+1} = \Delta \sqrt{\frac{b_i^{(0,0)} b_{i+1}^{(0,0)} U}{Z_0 g_1 g_2}}, \quad i = 1,2,3 \tag{8b}$$

$$\mathbf{J}_{56} = \sqrt{\frac{k^2 U}{Z_0^2 (1+k^2)}}, \quad \mathbf{J}_{67} = \frac{U}{Z_0}, \tag{8c}$$

$$\mathbf{J}_{57} = \frac{U}{\sqrt{Z_0^2 (1+k^2)}}, \quad \mathbf{J}_{78} = \frac{U}{\sqrt{k^2} Z_0}, \tag{8d}$$

where g_i denotes either Chebyshev or Butterworth filter prototype values [18], and Δ represents the fractional bandwidth of NRF-FPD at static state (without modulation). Similarly, $b_i^{(0,0)}$ represents the slope parameters of the time-modulated resonator at the resonant frequency (ω_0). The value of $b_i^{(0,0)}$ at ω_0 was expressed as follows:

$$b_i^{(0,0)} = \frac{\omega_0}{2}\frac{d\left[im\left(Y_{ini}^{0,0}\right)\right]}{d\omega}\bigg|_{\omega=\omega_0} \tag{9}$$

To achieve perfect isolation between the outports at f_0, the value of the isolation resistor ($R_{iso} = R_{iso}^{21} + R_{iso}^{31}$) was calculated by equating $\mathbf{S}_{22o}^{(k_1,k_2)}$ and $\mathbf{S}_{33o}^{(k_1,k_2)}$ to zero. The values of R_{iso}^{21} and R_{iso}^{31} were expressed as follows:

$$R_{iso}^{2,1} = Z_0, \quad R_{iso}^{3,1} = k^2 Z_0. \tag{10}$$

As seen in Eq. (5c)–(5d) and Eq. (6a)–(6d), the proposed power divider split the signal transmission between the output ports with an arbitrary PDR (i.e., $|S_{21}| = k/\sqrt{1+k^2}$, $|S_{31}| = 1/\sqrt{1+k^2}$) in the forward direction and those with a high reverse isolation (i.e., $|S_{12}| = |S_{13}| \approx 0$) in the backward direction. The time-modulated resonator generated IM products due to the mixing of the RF and modulation signals. These IM products transmitted through different transmission paths with distinct transmission phases. The phase difference ($\Delta\varphi$) in the progressive phase shift sinusoidal modulation played an important role in attaining a non-reciprocal response. In the absence of a modulation signal, the proposed circuit functions acted like a conventional reciprocal power divider (i.e., $|S_{21}| = |S_{12}| = k/\sqrt{1+k^2}$, $|S_{31}| = |S_{13}| = 1/\sqrt{1+k^2}$).

3. Modulation Parameter Selection

With the appropriate selection of modulation parameters (i.e., f_m, m, $\Delta\varphi$), the proposed power divider achieved low transmission loss in the forward direction and high reverse isolation in the backward direction. To achieve low transmission loss and high reverse isolation, parametric studies of the modulation parameters were performed, and the results are shown in Fig. 4. These results in Fig. 4 were obtained using the analytical design equations described in previous sections. The chosen circuit parameters of time-modulated resonators Z_1 = 70 Ω, Z_2 = 60 Ω, Z_b = 90 Ω, θ_0 = 16°, θ_1 = 40, θ_c = 25°, and C_{v0} = 6 pF, resulted in a resonant frequency of 1.80 GHz. The low pass prototype elements were calculated by considering a return loss of 26.40 dB in the Chebyshev response. The modulation parameters and results are summarized in Table 1. As shown in the Fig. 4, the proposed NR-FPD exhibited a filtering response with low IL in the forward direction and high isolation (ISO) in the backward direction.

When the modulation parameters were f_m = 89.64 MHz, m = 0.01543, and $\Delta\varphi$ = 60°, a reverse ISO (*i.e.*, $|S_{12}|$ and $|S_{12}|$) of higher than 45 dB was achieved at center frequency, however, the 20-dB ISO bandwidth is very narrow. When the modulation parameters were f_m = 93.96 MHz, m = 0.01984, and $\Delta\varphi$ = 32°, the forward transmission IL (IL = $|S_{21}|$ = $|S_{31}|$) in the forward direction was less than 0.84 dB (excluding the inherent PDR of power divider), the input port return loss ($|S_{11}|$) at passband exceeded 14 dB, and the isolation in the backward direction (i.e., $|S_{12}|$ and $|S_{13}|$) remained higher than 18 dB for RF frequencies from 1.5 GHz to 2.1 GHz. Although the NR-FPD did not contain any lossy elements, the small IL was attributable due to the power conversion into IM products at harmonics, which was not fully recovered to the fundamental frequency.

As depicted in Fig. 4(b) and 4(c), the backward transmission isolation bandwidth of 17 dB of the proposed NR-FPD was infinite. It should be noted that ultrawide reverse ISO bandwidth was attained when $\Delta\varphi$ = 32°. Fig. 5 shows the calculated frequency response for the NR-FPD with different fractional bandwidths. These results indicated that if a higher fractional bandwidth of NR-FPD is chosen, then higher values for the modulation frequency (f_m) and modulation index (m) should also be chosen.

The simulated results for the proposed NR-FPD shown in Fig. 6, demonstrate tunable frequency response. The frequency tunable response can be attained by adjusting the capacitor values (C_{v0}). The modulation parameters and the summary of simulated *S*-parameters are presented in Table 2. The frequency tunable range was from 1.64 GHz to 1.98 GHz with a worst-case IL (excluding the intrinsic loss of power divider) that was below 0.82 dB. In addition, the reverse ISO exceeded 18.4 dB across the entire operating frequency span.

III. SIMULATION AND MEASUREMENT RESULTS

For the experimental proof-of-concept, an NR-FPD with an equal PDR (k^2 = 1) was designed and fabricated. The NR-FPD prototype was fabricated using a Taconic substrate with a thickness of h = 0.787 mm and a dielectric constant of ε_r = 2.2. The proposed NR-FPD was designed with a fractional bandwidth of 6% and a passband return of 26.10 dB in the static state. The design objective was to obtain minimum IL and ultrawide high isolation in the backward direction while tuning the frequency from 1.60 GHz to 2 GHz. The time-modulated resonator was implemented by using transmission terminated with SMV1233-079LF varactor diode developed by Skyworks Inc. [19].

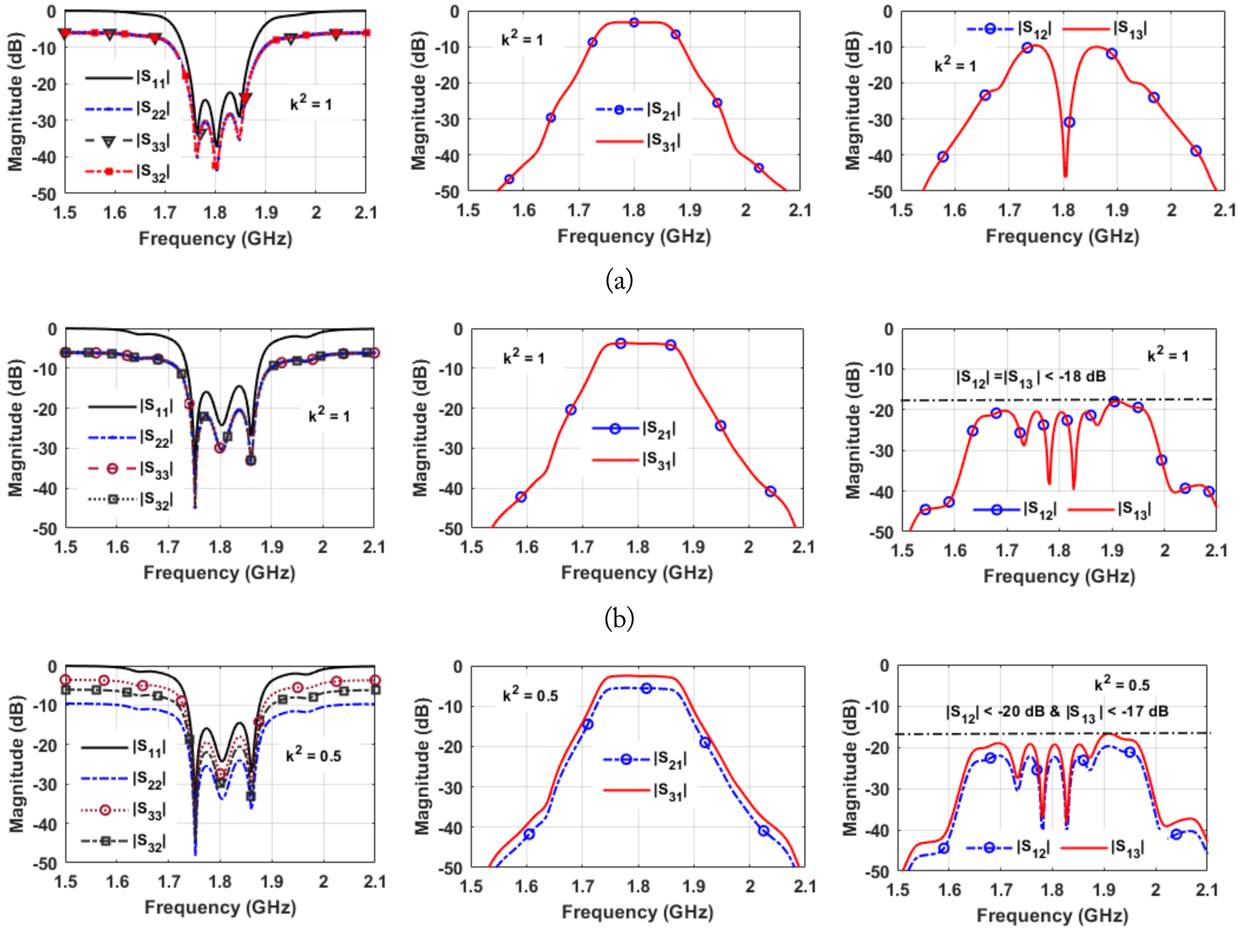

(a)

(b)

(c)

Fig. 4. Simulated S-parameters of the NR-FPD with various modulation parameters and power division ratios: (a) $k^2 = 1, f_m = 89.64$ MHz, $m = 0.01543$, $\Delta\varphi = 60°$, (b) $k^2 = 1, f_m = 93.96$ MHz, $m = 0.01984$, $\Delta\varphi = 32°$, and (c) $k^2 = 0.5, f_m = 93.96$ MHz, $m = 0.01984$, $\Delta\varphi = 32°$. The chosen prototype element values were: $g_0 = 1.0$, $g_1 = 0.7127$, $g_2 = 1.20041$, $g_3 = 1.32131$, $g_4 = 0.6477$, $g_5 = 1.10061$. The J-inverter values for $k^2 = 1$ and $\Delta = 6\%$ were as follows: $J_{s1} = J_{45} = 0.0050741$, $J_{12} = J_{34} = 9.91939\times10^{-4}$, $J_{23} = 7.2855\times10^{-4}$, $J_{56} = J_{57} = 0.01414$, and $J_{67} = J_{78} = 0.02$. The J-inverter values for $k^2 = 0.5$ and $\Delta = 6\%$ were as follows: $J_{s1} = J_{45} = 0.0050741$, $J_{12} = J_{34} = 9.91939\times10^{-4}$, $J_{23} = 7.2855\times10^{-4}$, $J_{56} = 0.011547$, $J_{67} = 0.023094$, $J_{57} = 0.02$, and $J_{78} = 0.02828$.

Table 1. Modulation parameters and summary of the simulated results

PDR	Fractional BW, Δ (%)	Modulation parameters			$\|S_{31}\|$ and $\|S_{21}\|$ (dB)	$\|S_{13}\|$ and $\|S_{12}\|$ within the passband (dB)	ISO BW (MHz)	
		f_m (MHz)	m	$\Delta\varphi$			$BW_{20dB\text{-}ISO}$	$BW_{18dB\text{-}ISO}$
$k^2 = 1$	6	89.64	0.01543	60°	3.27 / 3.27	>10 / 10	36	51
		93.96	0.01984	32°	3.82 / 3.82	>20 / 20	200	∞
	4	63.34	0.01310	32°	3.82 / 3.82	>20 / 20	220	∞
$k^2 = 0.5$	6	99.1	0.01984	32°	2.60 / 5.60	>19.5 / 20	200	∞

$BW_{20dB\text{-}ISO}$=bandwidth of $|S_{12}|$ and $|S_{13}|$ when their values were less than −20 dB, $BW_{18dB\text{-}ISO}$=bandwidth of $|S_{12}|$ and $|S_{13}|$ when their values were less than −18 dB.

Fig. 7 shows the overall circuit implementation of the proposed NR-FPD. J-inverters, namely $\mathbf{J_{s1}}$ and $\mathbf{J_{45}}$, were implemented using series transmission (W_a, L_a) and a coupled line (W_1, L_1, g_1). Similarly, coupling between the second and third resonators ($\mathbf{J_{12}}$) and between the third and fourth resonators ($\mathbf{J_{34}}$) was implemented using a short-circuited transmission (W_g, L_g). Additionally, the coupling between the second and third resonators was implemented using a coupled line (W_4, L_1, g_2).

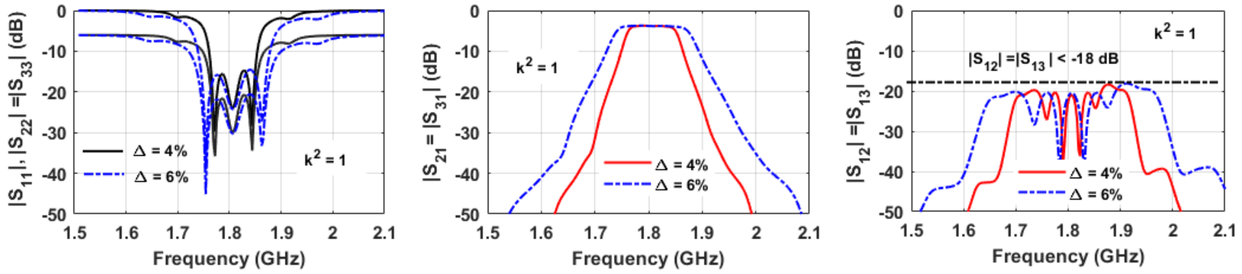

Fig. 5. Calculated S-parameters of NR-FPD with $k^2 = 1$ and various fractional bandwidths. The modulation parameters were $f_m = 93.96$ MHz, $m = 0.01984$, and $\Delta\varphi = 32°$. The chosen prototype element values were as follows: $g_0 = 1.0$, $g_1 = 0.71271$, $g_2 = 1.2004$, $g_3 = 1.32131$, $g_4 = 0.64771$, and $g_5 = 1.10061$. The J-inverter values were follows: $J_{s1} = J_{45} = 0.0050741$, $J_{12} = J_{34} = 9.91939\times10^{-4}$, $J_{23} = 7.2855\times10^{-4}$, $J_{56} = J_{57} = 0.01414$, and $J_{67} = J_{78} = 0.02$.

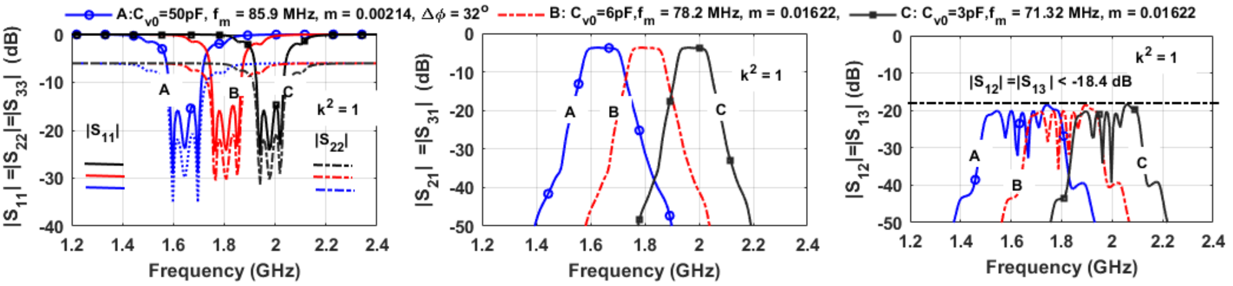

Fig. 6. Calculated S-parameters of NR-FPD with $k^2 = 1$ and frequency tunable characteristics. The chosen prototype values were as follows: $g_0 = 1.00$, $g_1 = 0.71271$, $g_2 = 1.20041$, $g_3 = 1.32131$, $g_4 = 0.64771$, and $g_5 = 1.10061$. The J-inverter values were as follows: $J_{s1} = J_{45} = 0.0050741$, $J_{12} = J_{34} = 9.91939\times10^{-4}$, $J_{23} = 7.2855\times10^{-4}$, $J_{56} = J_{57} = 0.01414$, and $J_{67} = J_{78} = 0.02$.

Table 2. Modulation parameters and summary of the simulated results

PDR	C_{v0} (pF)	Modulation parameters			f_0 (GHz)	$\|S_{21}\|$ / $\|S_{31}\|$ (dB)	Reverse ISO = $\|S_{12}\|$ = $\|S_{13}\|$ the within passband (dB)	ISO BW (MHz)	
		f_m (MHz)	m	$\Delta\varphi$				$BW_{20dB\text{-}ISO}$	$BW_{18dB\text{-}ISO}$
$k^2 = 1$	3	85.9	0.00214	32°	1.64	3.79 / 3.29	>20	36	∞
	6	78.02	0.01622	32°	1.81	3.78 / 3.78	>20	220	∞
	50	71.32	0.02978	32°	1.98	3.82 / 3.82	>20	200	∞

ISO=isolation, $BW_{20dB\text{-}ISO}$=bandwidth of $|S_{12}|$ and $|S_{13}|$ when their values were less than −20 dB, $BW_{18dB\text{-}ISO}$=bandwidth of $|S_{12}|$ and $|S_{13}|$ when their values were less than −18.4 dB.

Quarter-wavelength transmissions (W_p, L_p) were utilized for implementing J-inverters $\mathbf{J_{56}}$ and $\mathbf{J_{57}}$. In addition, another quarter-wavelength TLs (W_0, L_0) were employed to implement J-inverters $\mathbf{J_{67}}$ and $\mathbf{J_{78}}$. The DC-bias voltage and the progressive phase shift sinusoidal modulation signal were applied to the varactor diode through transmission (TL_{bias}: W_5 and L_5), as shown in Fig. 7. The simulation results were obtained using the ANSYS high frequency structure simulator and Keysight Advanced System Design (ADS). The equivalent circuit model of the SMV1233-079LF varactor diode provided by manufacture was used in harmonic balance simulation. For the measurement, the DC-bias voltage and sinusoidal modulation signals were supplied to the NR-FPD circuit using 33622A Keysight arbitrary wave generators, where the DC-bias voltage and phase shift of the modulation signals could be easily controlled.

The frequency response of the fabricated prototype was characterized by measuring the S-parameter results. Fig. 8 shows the measurement setup for the NR-FPD. The comparison between the simulation and experimental S-parameters of NR-FPD is depicted in Fig. 9. As shown in the figures, the experimentally characterized S-parameters were well aligned with the simulations. The measured S-parameters results are summarized in Table 3.

Although Fig. 9 depicts the S-parameters of the fabricated NR-FPD at three tunable frequency states (A, B, and C) only, it should be noted that the frequency response of the fabricated NR-FPD was altered between 1.620 GHz and 1.950 GHz by varying the bias voltage of the varactor diode. The measurement results show that the passband input return loss ($|S_{11}|$) remained higher than 12 dB, output return losses ($|S_{22}|$ and $|S_{33}|$) were

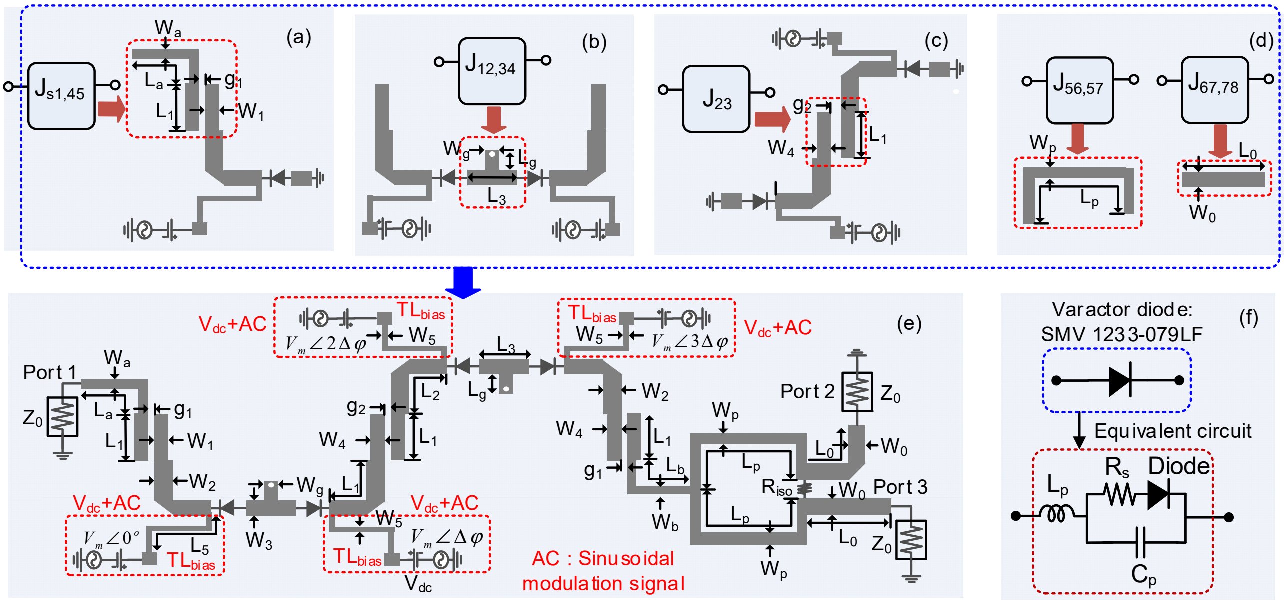

Fig. 7. Physical implementation of the NR-FPD with following dimensions: $W_a = W_b = 0.91$, $L_a = L_b = 12.21$, $g_1 = 0.12$, $W_1 = 1.04$, $L_1 = 10.78$, $W_2 = 1.37$, $L_2 = 16.02$, $L_3 = 11.96$, $W_g = 1.41$, $L_g = 1.51$, $W_4 = 1.72$, $g_2 = 1.13$, $W_5 = 0.61$, $L_5 = 24.10$, $W_p = 1.32$, $L_p = 32$, $W_0 = 2.40$, and $L_0 = 20$. The equivalent SPICE circuit model of the SMV1233-079LF varactor diode from Skyworks Inc. had parasitic resistance $R_s = 1.5\ \Omega$, inductance $L_p = 0.7$ nH, and $C_p = 0.5$ pF.

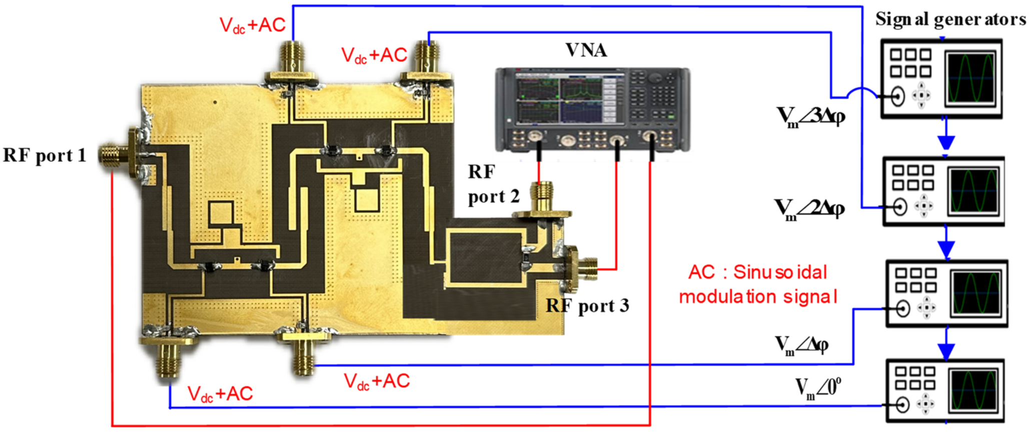

Fig. 8. Photograph of the fabricated NR-FPD with the measurement setup.

better than 15 dB and reverse ISO exceeded 19 dB. The transmission loss remained in the range of 4.31–5.41 dB (excluding the inherent 3.01 dB power division). These transmission losses occurred due to the parasitic resistance of varactor diodes. The parasitic resistance of the varactor diode increased at lower DC-bias voltages, causing the forward loss to increase slightly, while the frequency was tuned toward a lower frequency. The measurement also showed that the isolation of the two output ports (i.e., ($|S_{32}|$) was higher than 16 dB at the passband center frequencies. Due to cross-coupling resulting from the progressive phase shifted sinusoidal modulation signal, transmission zeros (TZs) appeared in the forward direction of transmission, as shown in Fig. 9. When resonators were modulated with the progressive phase shift sinusoidal signal, IM products were generated. As a result, the RF power signal was distributed among the IM products, and transversal propagation of the RF signal occurred not only through the fundamental frequency, but also through non-adjacent resonators at harmonic frequencies. This phenomenon led to the generation of TZs.

To investigate the cause of the forward transmission IL, we performed a simulation of the NR-FPD using the SPICE model of SMV 1233-079LF varactor diode from Skyworks Inc. The results shown in Fig. 10 indicate that the forward transmission IL was mainly due to the parasitic resistance (R_S) of the varactor diode. As the value of R_S increased, the forward transmission IL also increased. Therefore, the IL can be reduced if a varactor diode with lower parasitic resistance (high *Q*-factor varactor diode) is used.

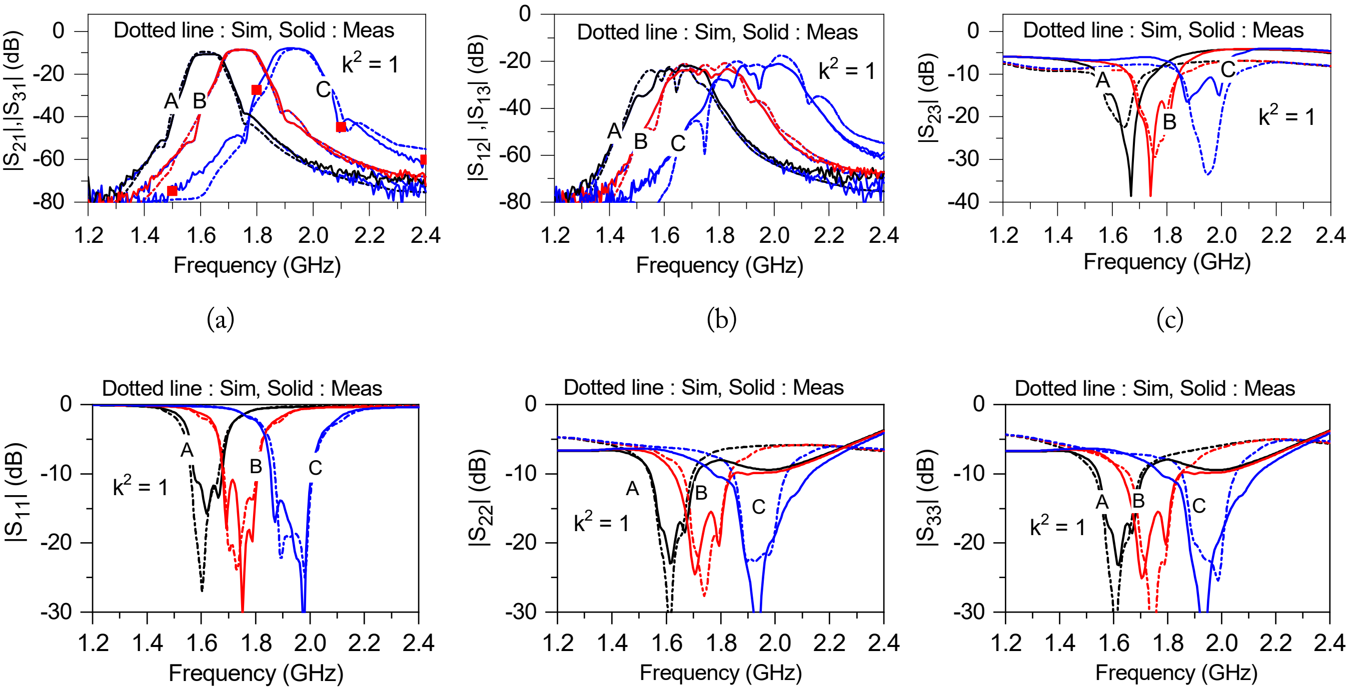

(a) (b) (c)

(d) (e) (f)

Fig. 9. Simulation and experimental *S*-parameters results for the fabricated NR-FPD with a tunable frequency: (a) $|S_{21}|$, $|S_{31}|$, (b) $|S_{12}|$, $|S_{13}|$, (c) $|S_{23}|$, (d) $|S_{11}|$, (e) $|S_{22}|$, and (f) $|S_{33}|$.

Table 3. Measured results for the NR-FPD with an equal power division ratio ($k^2 = 1$)

	Tunable frequency state		
	A	B	C
Modulation parameters			
f_m (MHz)	80	88	88
V_m (V)	2	2.70	3.20
$\Delta\varphi$ (°)	35	36	37
Measured results			
V_{dc} (V)	0	2.40	6
f_0 (GHz)	1.62	1.75	1.95
$\|S_{11}\| / \|S_{22}\| / \|S_{33}\|$ (dB)	>11.6 / 17.02 / 17.2	>10.90 / 15.5 / 15.45	>14.4 / 17.1 / 17.2
$\|S_{21}\| / \|S_{31}\|$ @ f_0 (dB)	8.71 / 8.73	8.10 / 8.11	7.56 / 7.58
$\|S_{21}\|$ and $\|S_{31}\|$ (dB)	>21.60	>23.40	>21.20
$\|S_{32}\|$ @ f_0 (dB)	18.2	22.20	12.1
Insertion loss (dB)	<5.70	<5.09	<4.55
ISO @ f_0 (dB)	22.89	24.24	22.90
ISO @ all frequency (dB)	>20.6	>20.40	>21.20
BW_{3dB} (MHz)	110	120	131
$BW_{20dB\text{-}ISO}$ (MHz)	All freq (∞)	All freq (∞)	All freq (∞)
Frequency tunability range	1.62–1.95 GHz (0.33 GHz): 18.48%		

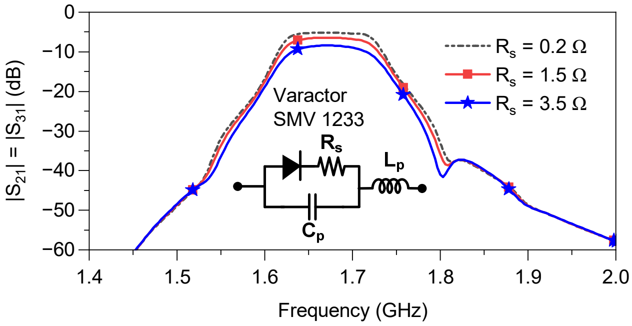

Fig. 10. Simulated results for the NR-FPD with different parasitic resistance (R_s) values of the varactor diode.

Table 4 compares the performance of the proposed NR-FPD with those described in previously published works [14–17]. Notably, these previously reported NR-FPDs [14–17] exhibited a high reverse ISO only at the center frequency and the 20-dB isolation bandwidth remained between 5 and 96 MHz. In contrast, this paper proposes an NR-FPD with frequency tunability and an ultrawide high reverse ISO bandwidth. The experimental results show that attenuation exceeded 20 dB in the reverse direction for all operating frequency ranges.

IV. CONCLUSION

This paper proposes a novel design of a multi-functional NR-FPD that combines the functions of a tunable bandpass filter, a power divider with an arbitrary PDR, and an isolator into one circuit. The achievement of an ultrawide high reverse isolation bandwidth was facilitated by properly selecting the modulation parameters of the time-modulated resonators. Moreover, the proposed NR-FPD features a low transmission IL in the forward direction and ultrawide high reverse isolation bandwidth in the backward direction, with tunable frequency functionalities. To validate the performance experimentally, a prototype of the NR-FPD was designed. The results show that the measured *S*-parameters had excellent agreement with the simulation.

This work was supported in part by the National Research Foundation of Korea (NRF) grant funded by Korean government (MSIT) (Grant No. RS-2023-00209081, 40%); in part by the Basic Science Research Program through NRF of Korea funded by the Ministry of Education (Grant No. RS-2019-NR040079, 40%); and in part by the Institute of Information & Communications Technology Planning & Evaluation (IITP)–Innovative Human Resource Development for Local Intellectualization Program grant funded by Korean government (MSIT) (Grant No. IITP-2024-RS-2024-00439292, 20%).

REFERENCES

[1] X. B. Zhao, F. Wei, P. F. Zhang, and X. W. Shi, "Mixed-mode magic-Ts and their applications on the designs of dual-band balanced out-of-phase filtering power dividers," *IEEE Transactions on Microwave Theory and Techniques*, vol. 71, no. 9, pp. 3896-3905, 2023. https://doi.org/10.1109/TMTT.2023.3253567

[2] X, B. Zhao, F. Wei, and X. Liu, "Balanced-to-single-ended filtering power divider using multilayer mixed-mode magic-T," *IEEE Transactions on Circuits and Systems II: Express Briefs*, vol. 70, no. 8, pp. 2859-2863, 2023. https://doi.org/10.1109/TCSII.2023.3247862

[3] A. Jaiswal, M. P. Abegaonkar, and S. K. Koul, "Impedance transformer for recessed ground patch antenna at 60 GHz," *IEEE Antennas and Wireless Propagation Letters*, vol. 18, no. 10, pp. 2036-2040, 2019. https://doi.org/10.1109/LAWP.2019.2936770

[4] C. E. Fay and R. L. Comstock, "Operation of the ferrite junction circulator," *IEEE Transactions on Microwave Theory and Techniques*, vol. 13, no. 1, pp. 15-27, 1965. https://doi.org/10.1109/TMTT.1965.1125923

[5] C. K. Seewald and J. R. Bray, "Ferrite-filled antisymmetrically biased rectangular waveguide isolator using magnetostatic surface wave modes," *IEEE Transactions on Microwave Theory and Techniques*, vol. 58, no. 6, pp. 1493-1501, 2010. https://doi.org/10.1109/TMTT.2010.2047919

Table 4. Performance comparison with previously published works

Study	FTR (GHz)	No. of TVR	IL (dB)	RL (dB)	ISO @ f_0 (dB)	BW_{3dB} (MHz)	$BW_{20dB\text{-}ISO}$ (MHz)	Circuit size
Chaudhary et al. [14]	1.46	2	2.94	>15	28.77	130	50	$0.80\lambda_g \times 0.34\lambda_g$
Zhao et al. [15]	2.38–2.42 (1.66%)	5	4.8–5.9	>12	19.2–24	NA	5	$2.72\lambda_g \times 2.72\lambda_g$
Zang et al. [16]	2.45	6	8	>12	6.8–62.1	90	NA	NA
Chaudhary and Jeong [17]	1.66–1.98 (17.5%)	6	3.88–5.04	>11.44	20.2	100–112	70–96	$0.62\lambda_g \times 0.32\lambda_g$
This work	1.62–1.95 (18.48%)	4	4.55–5.70	>10.9	23.4–31.2	110–131	∞	$0.63\lambda_g \times 0.41\lambda_g$

[6] X. Wu, X. Liu, M. D. Hickle, D. Peroulis, J. S. Gomez-Diaz, and A. A. Melcon, "Isolating bandpass filters using time-modulated resonators," *IEEE Transactions on Microwave Theory and Techniques*, vol. 67, no. 6, pp. 2331-2345, 2019. https://doi.org/10.1109/TMTT.2019.2908868

[7] G. Chaudhary and Y. Jeong, "Non-magnetic non-reciprocal bandpass filter with quasi-elliptic response and tunable center frequency," *AEU-International Journal of Electronics and Communications*, vol. 175, article no. 155111, 2024. https://doi.org/10.1016/j.aeue.2023.155111

[8] A. Alvarez-Melcon, X. Wu, J. Zang, X. Liu, and J. S. Gomez-Diaz, "Coupling matrix representation of nonreciprocal filters based on time-modulated resonators," *IEEE Transactions on Microwave Theory and Techniques*, vol. 67, no. 12, pp. 4751-4763, 2019. https://doi.org/10.1109/TMTT.2019.2945756

[9] G. Chaudhary and Y. Jeong, "Nonreciprocal bandpass filter using mixed static and time-modulated resonators," *IEEE Microwave and Wireless Components Letters*, vol. 32, no. 4, pp. 297-300, 2022. https://doi.org/10.1109/LMWC.2021.3123306

[10] Z. Zhang and D. Psychogiou, "Incorporating directionality in transversal-resonator-based bandpass filters with tunable transfer function characteristics," *IEEE Transactions on Circuits and Systems I: Regular Papers*, vol. 70, no. 12, pp. 5194-5207, 2023. https://doi.org/10.1109/TCSI.2023.3320036

[11] P. Dutta, G. A. Kumar, and G. Ram, "Numerical design of non-reciprocal bandpass filters with the aid of 3D coupling matrix for 5G bands," *IEEE Transactions on Circuits and Systems II: Express Briefs*, vol. 69, no. 7, pp. 3334-3338, 2022. https://doi.org/10.1109/TCSII.2022.3157644

[12] G. Chaudhary and Y. Jeong, "Frequency tunable impedance matching nonreciprocal bandpass filter using time-modulated quarter-wave resonators," *IEEE Transactions on Industrial Electronics*, vol. 69, no. 8, pp. 8356-8365, 2022. https://doi.org/10.1109/TIE.2021.3106023

[13] G. Chaudhary and Y. Jeong, "Rigorous design and experimental validation of non-reciprocal bandpass filter with ultrawide high reverse isolation bandwidth," *Engineering Science and Technology, an International Journal*, vol. 52, article no. 101674, 2024. https://doi.org/10.1016/j.jestch.2024.101674

[14] G. Chaudhary, P. Pech, S. Saron, D. Psychogiou, and Y. Jeong, "Nonreciprocal filtering power divider using mixed static and time-modulated resonators: numerical design approach and experimental validation," in *Proceedings of 2023 53rd European Microwave Conference (EuMC)*, Berlin, Germany, 2023, pp. 90-93. https://doi.org/10.23919/EuMC58039.2023.10290566

[15] D. Zhao, F. Lin, and H. Sun, "Frequency-tunable nonreciprocal SIW filtering power divider using a common resonator with mixed static and time-modulated degenerate modes," *IEEE Transactions on Microwave Theory and Techniques*, vol. 72, no. 9, pp. 5430-5440, 2024. https://doi.org/10.1109/TMTT.2024.3370153

[16] J. Zang, S. Wang, A. Alvarez-Melcon, and J. S. G. Diaz, "Nonreciprocal filtering power dividers," *AEU-International Journal of Electronics and Communications*, vol. 132, article no. 153609, 2021. https://doi.org/10.1016/j.aeue.2021.153609

[17] G. Chaudhary and Y. Jeong, "Unequal power division ratio nonreciprocal filtering power divider with arbitrary termination impedance and center frequency tunability," *IEEE Transactions on Microwave Theory and Techniques*, vol. 72, no. 1, pp. 242-251, 2024. https://doi.org/10.1109/TMTT.2023.3288635

[18] R. J. Cameron, C. M. Kudsia, and R. R. Mansour, *Microwave Filters for Communication Systems: Fundamentals, Design, and Applications*. Hoboken, NJ: John Wiley & Sons, 2007.

[19] Skyworks Solution Inc., "SMV123x series: hyperabrupt junction tuning varactors," 2020 [Online]. Available: https://www.skyworksinc.com/en/Products/Diodes/SMV1231-Series.

Girdhari Chaudhary

https://orcid.org/0000-0003-2060-9860

received his B.E. in electronics and Communication Engineering from Nepal Engineering College (NEC), Kathmandu, Nepal, in 2004 and his M. Tech. in electronics and Communication Engineering from MNIT, Jaipur, India in 2007 and his PhD in Electronics Engineering from Jeonbuk National University, Republic of Korea in 2023. He is currently working as a research associate professor at the Jeonbuk RICE Intelligence Innovation Research Center, Jeonbuk National University, South Korea. He worked as a research assistant professor at Jeonbuk National University under a Korean Research Fellowship program called the Brain Pool Program from Oct 2016 to March 2021. From March 2021 to August 2024, he worked as contract professor at the JIANT-IT Human Resource Development Center, Jeonbuk National University, Korea. He was also the Principal Investigator (PI) for an independent Project through the Basic Science Research Program of the National Research Foundation (NRF), funded by the Ministry of Education Korea. In addition, he received the BK21 PLUS Research Excellence Award in 2015 and a Korean Research Fellowship (KRF) through the National Research Foundation (NRF) of Korea, funded by the Ministry of Science and ICT. His research interests include multi-band tunable passive circuits, in-band full duplex systems and high efficiency power amplifiers, and negative group delay circuits and their applications.

Daewoo Choi

https://orcid.org/0009-0008-4355-953X

received his Bachelor's, Master's and doctoral degrees in Industrial Engineering from Jeonbuk National University, Jeonju, Republic of Korea in 1997, 1999, and 2004, respectively. His professional career encompasses significant contributions to the research departments of prominent organizations, including the KT Central Research Center. In 2022, he became a faculty member at the Graduate School of Convergence Technology and Management at Jeonbuk National University, where he continues to pursue his academic endeavors. At Jeonbuk National University, he has been involved in the planning and execution of various institutional initiatives, such as the BK21 FOUR program and the RIS project. His primary research interests include the analysis of big data derived from microwave technology and the commercialization of microwave applications in the agricultural and life sciences domains. His work extends to research on plant growth and preservation utilizing microwave technology, and he collaborates with a range of corporate partners to develop Research and Business Development (R&BD) strategies aimed at commercializing these technologies in regions such as Central Asia and Middle East.

Yongchae Jeong

https://orcid.org/0000-0001-8778-5776

received his BSEE and MSEE, and Ph.D. degrees in electronics engineering from Sogang University, Seoul, Republic of Korea in 1989, 1991, and 1996, respectively. From 1991 to 1998, he worked as a senior engineer with Samsung Electronics, Korea. From 1998, he joined the Division of Electronics Engineering at Jeonbuk National University, Jeonju, Republic of Korea. From July 2006 to December 2007, he was as a visiting Professor at Georgia Institute of Technology, United States. Since July 2024, he has been the Director of the Jeonbuk RICE Intelligence Innovation Research Center, Jeonbuk National University. He is a professor and a member of the IT Convergence Research Center. He also served the as Vice-President of Plan Affairs and the Director of the HOPE-IT Human Resource Development Center of BK21 PLUS, Jeonbuk National University. He is teaching and conducting research on microwave passive and active circuits, mobile and satellite base-station RF systems, design of periodic defected transmission line, negative group delay circuits and their applications, in-band full duplex radio, and RFIC design. He is a senior member of IEEE and a member of Korea Institute of Electromagnetic Engineering and Science (KIEES). He has authored and co-authored over 250 papers in international journals and conference proceedings.